Intensity Inhomogeneity Correction for Large Panoramic Electron Microscopy Images

Oleh Dzyubachyk[1,2(✉)], Abraham J. Koster[2], and Boudewijn P. F. Lelieveldt[1,3]

[1] Division of Image Processing, Department of Radiology, Leiden University Medical Center, Leiden, The Netherlands

[2] Section Electron Microscopy, Department of Cell and Chemical Biology, Leiden University Medical Center, Leiden, The Netherlands
o.dzyubachyk@lumc.nl

[3] Pattern Recognition and Bioinformatics Lab, Delft University of Technology, Delft, The Netherlands

Abstract. In various medical and biological modalities, in particular, electron microscopy (EM), visualization of large fields of view requires acquisition of multiple overlapping frames with their subsequent reconstruction into a single panoramic image. Such reconstruction process is hampered by several factors, including different intensity scaling and imperfect localization of the acquired frames, intensity inhomogeneity within each frame, and large content variability between different frames. This poses a significant challenge not only for visualization, but also for further quantification of such panoramic images. In this work, we present a simple yet efficient data-driven algorithm that improves reconstruction of the large panoramic views using a minimal set of assumptions. More precisely, our approach fully relies on the information from the overlap regions of the neighbouring frames. Such formulation results in a linear system of equations that can be solved numerically, when supported by proper constraints. We validated our approach on a large set of highly-diverse in-house EM panoramic views and demonstrated improved performance with respect to traditional metrics as well as network training capacity.

Keywords: Panoramic image · Electron microscopy · Intensity inhomogeneity correction · Intensity standardization

1 Introduction

For many different medical and biological modalities, including light and electron microscopy (EM), pathology, and magnetic resonance imaging, the size of a sample being visualized is limited by the physical size of the imaging device.

Supplementary Information The online version contains supplementary material available at https://doi.org/10.1007/978-3-031-77786-8_5.

Y. Huo et al. (Eds.): MOVI 2024, LNCS 15371, pp. 45–54, 2025.
https://doi.org/10.1007/978-3-031-77786-8_5

Hence, larger fields of view are acquired in multiple stages, which requires subsequent reconstruction (stitching) of the acquired frames into a single picture. Such panoramic views, being a collection of separately-acquired images, inevitably suffer from intrinsic imperfections, including: different intensity scaling of the acquired frames, intensity inhomogeneity (bias) within each frame, imperfect localization of each separate frame, and large content variability between different frames. All these factors hamper subsequent quantification of the panoramic images.

Improved stitching of the EM data has recently received significant attention [1,7,10,12,14]. However, the vast majority of these methods concentrate on compensation of misalignments and geometric distortions, and the size of the reconstructed stitches in terms of the number of frames remains rather low. In particular, Kaynig et al. [7] developed a method for correcting lens distortion for transmission EM images based on estimating the correspondences between SIFT landmarks. Bria et al. [1] present TeraStitcher, a tool specially developed for stitching of teravoxel-sized microscopy images. Scheffer et al. [12] present a multi-step approach for reconstructing EM stitches, with prior intensity normalization to a mix of two Gaussian distributions. Zheng et al. [14] developed a high-throughput EM platform for reconstructing the entire brain of the adult *Drosophila melanogaster*. Recently, Mahalingam et al. [10] built on the aforementioned work to develop a modular ASAP (Assembly Stitching and Alignment Pipeline) framework capable of reconstructing petabyte-sized data sets.

Two of the more recent approaches, MIST [2] and ASHLAR [11] are capable of dealing with larger microscopy panoramic images, but these approaches also do not perform intensity correction. In particular, the MIST algorithm of Chalfoun et al. [2] estimates translation between the pairs of the overlapping frames based on the phase correlation, with consequent estimation of the camera angle and hardware-related parameters. Recently, in their ASHLAR software tool, Muhlich et al. [11] extended this approach by using a spanning tree of the neighbourhood graph for joint estimation of the frame translations between the overlapping frames.

At the same time, reconstructed panoramic images presented in the publications and EM data analysis efforts, such as the MitoEM Challenge [6], exhibit clear stitching artefacts at the transitions between the overlapping frames. Correcting these artefacts will not only improve the visual appearance of these stitches, but will also lead to a more objective quantification. To the best or our knowledge, except for the learning-based solution developed specifically for relatively small histopathological stitches [8], our earlier work [4] is the only publication presenting a solution to this challenging problem.

In our recent publication [4], we presented a method capable of correcting and standardizing intensity of EM stitches and analyzed learning capacity of the corrected data. However, this solution turned out to be impractical when applied to really large stitches composed of few thousand separate frames.

Here we present a simple and efficient data-driven approach for correcting intrinsic intensity inhomogeneity within (large) panoramic images and analyze

Table 1. Number of annotated frames and different EM structures of interest from each selected data set

Number/Data set	2922Q1	2922Q4	2929L4	2929Q1	2929Q4
Frames	20	44	58	251	55
Mitochondria	222	598	1927	2764	745
Cell nuclei	0	17	37	122	39
Ruffled border	8	19	29	46	13

its performance on large collection of EM stitches. Our approach results in a system of linear equations that can be solved numerically. Since our method relies on the joint estimation of the correction parameters based on the average intensity in the overlap region, it does not require perfect alignment between the neighbouring frames. Hence, our approach can be easily combined with any of the reconstruction methods that improve alignment between the frames and perform geometric corrections.

Improved performance enabled by our approach has been demonstrated using both statistics in the overlap area as well as better convolutional neural network training. Moreover, this approach can be directly extended to different types of panoramic images, such as histopathology data or whole-body magnetic resonance volumes.

2 Data

For validation of our method, we selected 56 data sets from our in-house data repository acquired as part of the same project. All acquisitions were performed on a digital camera (One View, Gatan Inc., Pleasanton, CA, USA) mounted on a 120 kV transmission electron microscope (Tecnai T12 with a twin objective lens; Fei, Eindhoven, The Netherlands). The frames were acquired with 20% overlap, using the previously described protocol [4,5]. The number of frames per data set varied between 756 and 6236. For five representative data sets, three different structures: mitochondria, cell nucleus and ruffled border, were annotated by three experts in EM imaging, one data set by one expert, using custom in-house annotation software. Typical images from each of the data sets and the corresponding annotations are shown in Fig. 1. Total numbers of annotated frames and object instances are provided in Table 1. Supplementary Fig. 1 illustrates two of the five stitches selected for annotation, together with the corresponding regions of interest. Notably, the "2929L4" stitch exhibits a strong intensity gradient.

3 Methods

For each data set consisting of N_F frames, we denote the raw image intensity of frame $n = \overline{1, N_F}$ as $I_n(\mathbf{x})$ and the corrected intensity as $J_n(\mathbf{x}) = T(I_n(\mathbf{x})) - B(\mathbf{x})$.

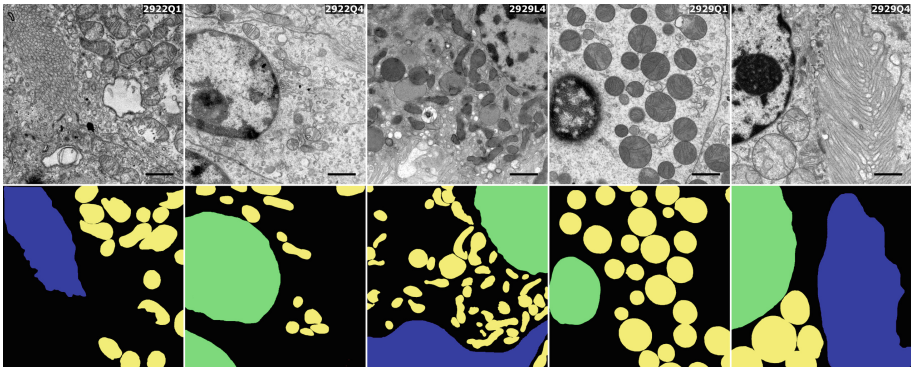

Fig. 1. Sample image from each data set and the corresponding annotation. Mitochondria, cell nuclei and ruffled border annotations are shown in yellow, green and blue, respectively. Contrast of the images was increased for visualization purposes. The length of the scale bar is 1 µm (Color figure online).

Here $T(I)$ is an intensity transformation function, $\mathbf{x}$ are Cartesian coordinates, and $B(\mathbf{x})$ is an intensity inhomogeneity field, common for all the frames. Inspired by [9], we model it as a weighted sum of N_G basis functions $\mathbf{G}(\mathbf{x})$:

$$B(\mathbf{x}) = \mathbf{w}^T \mathbf{G}(\mathbf{x}),$$

with $\mathbf{w} \in \mathbb{R}^{N_G}$ being the weights vector. Further, let $\mathcal{O}_{m;n}$ denote the region within the stack $\mathcal{O}_m$ where it overlaps with the stack $\mathcal{O}_n$, and $\overline{I}_{m;n}$, $\overline{J}_{m;n}$, and $\overline{\mathbf{G}}_{m;n}$ be, respectively, the average value of the raw image intensity, corrected image intensity, and basis functions within $\mathcal{O}_{m;n}$. Let the function

$$D^{(H)}_{m;n} = \overline{H}_{m;n} - \overline{H}_{n;m}$$

denote the difference between the mean intensity of the images H_n and H_m in the corresponding overlap areas. Denoting by $\mathcal{P}$ the set of all the N_P ordered pairs of the neighbouring frames, we define the following optimization function:

$$\begin{aligned} L &= \sum_{(m,n)\in\mathcal{P}} \left[D^{(J)}_{m;n}\right]^2 = \sum_{(m,n)\in\mathcal{P}} \left[\overline{J}_{m;n} - \overline{J}_{n;m}\right]^2 \\ &= \sum_{(m,n)\in\mathcal{P}} \left[\overline{T(I)}_{m;n} - \overline{T(I)}_{n;m} - \mathbf{w}^T \mathbf{D}^{(\mathbf{G})}_{m;n}\right]^2. \end{aligned} \tag{1}$$

In this work, we consider two simple cases for the intensity transformation function $T(I)$, namely: the additive model $T(I_n) = a_n + I_n$ parameterized by the intensity shift vector $\mathbf{a} \in \mathbb{R}^{N_F}$ and the multiplicative model $T(I_n) = s_n I_n$ parameterized by the intensity scaling vector $\mathbf{s} \in \mathbb{R}^{N_F}$.

3.1 Multiplicative Model

For the multiplicative model, we rewrite the optimization function defined in Eq. 1 as follows:

$$L^{(M)} = \sum_{(m,n)\in\mathcal{P}} \left[s_m \overline{I}_{m;n} - s_n \overline{I}_{n;m} - \mathbf{w}^T \mathbf{D}^{(\mathbf{G})}_{m;n} \right]^2. \tag{2}$$

Differentiating this function with respect to the scaling vector $\mathbf{s}$ and the bias field weights $\mathbf{w}$ results in the following system of matrix equations:

$$\begin{cases} \left[\mathbf{V}\mathbf{s} - \mathbf{w}^T \mathbf{D}^{(\mathbf{G})} \right]^T \mathbf{V} = \mathbf{0}, & (3) \\ \left[\mathbf{V}\mathbf{s} - \mathbf{w}^T \mathbf{D}^{(\mathbf{G})} \right]^T \mathbf{D}^{(\mathbf{G})} = \mathbf{0}, & (4) \end{cases}$$

where

$$\mathbf{V} = (v_{ij}) \in \mathbb{R}^{N_P \times N_G}, \qquad v_{ij} = \begin{cases} \overline{I}_{i;j}, & (i,j) \in \mathcal{P}, \\ -\overline{I}_{j;i}, & (j,i) \in \mathcal{P}, \\ 0, & \text{otherwise.} \end{cases}$$

Equations 3 and 4 together constitute a linear system of $N_F + N_G$ equations for calculating the same number of the unknowns: intensity scaling vector $\mathbf{s} \in \mathbb{R}^{N_F}$ and vector of bias field weights $\mathbf{w} \in \mathbb{R}^{N_G}$. However, it can be easily noticed that this system has a trivial solution. To overcome this, we constrain our optimization problem by the following condition:

$$\overline{J}_{n\in F_*} = \overline{\mathbf{I}}, \tag{5}$$

meaning that the average corrected intensity of the subset of frames F_* is equal to that of the entire stitch. This constraint is incorporated into our model as an additional term into the optimization function:

$$L_{\text{constr}} = L + \sum_{n\in F_*} (\overline{J}_n - \overline{\mathbf{I}})^2,$$

which results in the following modification of Equation 3:

$$\left[\mathbf{V}\mathbf{s} - \mathbf{w}^T \mathbf{D}^{(\mathbf{G})} \right]^T \mathbf{V} + \left[\Delta \mathbf{1}_{F_*} \mathbf{s} - \mathbf{1}_{F_*} \right] \overline{\mathbf{I}} = \mathbf{0}, \tag{6}$$

with $\mathbf{1}_{F^*} \in \mathbb{R}^{N_F}$ being the indicator function of the set F_* and Δ denoting the functor that distributes the elements of a vector along the diagonal of the corresponding square matrix. The resulting system of Equations 4 and 6 can be easily solved numerically.

3.2 Additive Model

For the additive model, we rewrite the optimization function defined in Eq. 1 as:

$$L^{(A)} = \sum_{(m,n)\in\mathcal{P}} \left[a_m + \overline{I}_{m;n} - a_n - \overline{I}_{n;m} - \mathbf{w}^T\mathbf{D}^{(\mathbf{G})}_{m;n}\right]^2. \tag{7}$$

Differentiating this function with respect to the shift vector $\mathbf{a}$ and the bias field weights $\mathbf{w}$, we arrive at the following counterparts of the Equations 3 and 4:

$$\begin{cases} \left[\mathbf{U}\mathbf{a} - \mathbf{w}^T\mathbf{D}^{(\mathbf{G})} + \mathbf{D}^{(\mathbf{I})}\right]^T \mathbf{U} = \mathbf{0}, & (8) \\ \left[\mathbf{U}\mathbf{a} - \mathbf{w}^T\mathbf{D}^{(\mathbf{G})} + \mathbf{D}^{(\mathbf{I})}\right]^T \mathbf{D}^{(\mathbf{G})} = \mathbf{0}, & (9) \end{cases}$$

where

$$\mathbf{U} = (u_{ij}) \in \mathbb{R}^{N_P \times N_G}, \qquad u_{ij} = \begin{cases} 1, & (i,j) \in \mathcal{P}, \\ -1, & (j,i) \in \mathcal{P}, \\ 0, & \text{otherwise.} \end{cases}$$

Similarly to the multiplicative model case, we need to constrain the above system as it can be easily proven that it is ill-conditioned due to particular form of the matrix $\mathbf{U}$. Adding the constraint defined in Eq. 5, we rewrite Equation 8 as:

$$\left[\mathbf{U}\mathbf{a} - \mathbf{w}^T\mathbf{D}^{(\mathbf{G})} + \mathbf{D}^{(\mathbf{I})}\right]^T \mathbf{U} + \Delta\mathbf{1}_{F_*}\mathbf{a} + \mathbf{1}_{F_*} \circ (\mathbf{I} - \overline{\mathbf{I}}) = \mathbf{0}, \tag{10}$$

which allows solving the resulting system of Equations 9 and 10 numerically; here $\circ$ denotes the Hadamard product between two vectors.

4 Experiments and Results

Our algorithm was implemented in Matlab R2019b (MathWorks; Natick, MA, USA) in the low-memory fashion as it simultaneously stores maximum 2 frames in the memory. The bias field was modelled using the polynomial basis functions; we will further refer to the highest degree of the polynomial basis function as the "order" of the corresponding model. Further, in all our experiments, the regularization set F_* consisted of ten frames with the highest information content in terms of the entropy. Neighbouring frames were labelled as overlapping if their overlap area was larger than 5% of the frame size. Statistical significance was assessed using the paired Student's test.

Training of the neural networks was implemented in Tensorflow v2.0.0. Architecture of the convolutional neural network was adapted from [13] for performing multi-class segmentation. Geometric data augmentation (flipping, rotation by 90°, 180° and 270°) was used at both training and testing phases. The dropout

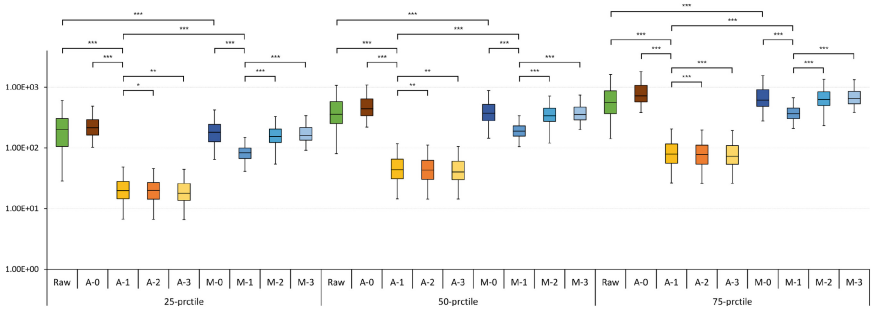

Fig. 2. The mean intensity difference in the overlap area of the neighbouring images, before and after correction. Here "A-[Q]" and "M-[Q]" denote intensity correction with the additive or multiplicative model of order Q, respectively. Whiskers of the boxplot indicate the maximum and the minimum value, respectively. The vertical axis is shown in the logarithmic scale.

rate was set to 0.1 and the batch size was set to 8. The network was trained for 50 epochs, using the weighted sum of the categorical cross-entropy and the Jaccard index as the loss function. The ratio between the sizes of the training and validation sets was 4:1. Prior to training, all frames were downsampled to the size of 256×256 pixels and all the stitches, both raw and intensity-corrected, were mapped to the same intensity space by using the exact histogram specification approach [3,4].

We start by analyzing the performance of our approach with respect to different models and complexity of the bias field. To objectively analyze these complex data, spanning over all the data sets and all the pairs of the overlapping frames within each data set, we calculated different percentiles $P(\left|D^{(i)}\right|)$ of the distribution

$$\left\{\left|D^{(i)}_{m;n}\right|\right\}\Big|_{(m,n)\in\mathcal{P}} \quad \text{for} \quad i \in \left\{I, J^{(A\text{-}[Q])}, J^{(M\text{-}[Q])}\right\} \text{ and } Q = \overline{0,3}.$$

Box-whisker plots presenting distributions of $P(\left|D^{(i)}\right|)$ over all the validation data sets are reported in Fig. 2. The reported results indicate that applying intensity correction using the linear model, with linear (first-order) polynomial bias field, has, in both cases, significantly lower loss compared to the raw data and other orders. Moreover, the fact that the constant model, without correction of the bias field, in both cases, performs worse than the linear one, confirms the added value of the bias field correction within each frame. This conclusion is in line with the results reported in [4].

Next, we assessed how the applied intensity correction impacts the neural network training ability, using the aforementioned network design. This experiment was implemented in the leave-one-set-out manner, meaning that one of the five annotated data sets was interchangeably used as the testing set and the network was trained on the remaining four. Each experiment was repeated four times, using different seeds for splitting the data into the training and validation parts, with five repetitions for each seed. The results in terms of the average

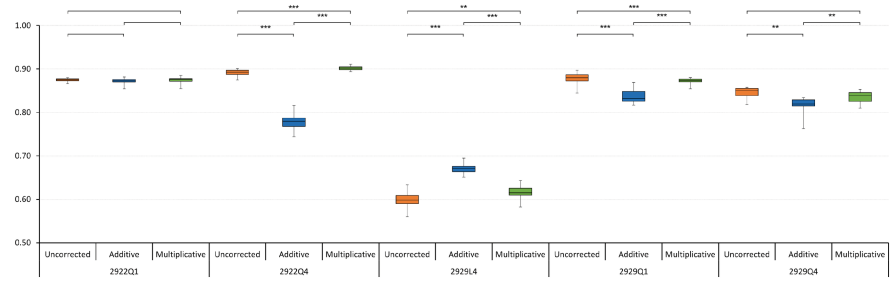

Fig. 3. Network training performance in terms of the Jaccard index on the test set for uncorrected and corrected data. The results were obtained in the leave-one-set-out manner, with 4 different seeds for data splitting and repeating each experiment for 5 times. Whiskers of the boxplot indicate the maximum and the minimum value, respectively.

Jaccard index on the three structures of interest on the test set are reported in Fig. 3.

For the final experiment, to demonstrate the added value of the bias correction, we have trained the network on all the five annotated data sets and applied it to a complete large unseen data set. The segmentation results for the three classes of interest on the data corrected by the zero-order (only scaling, no bias correction) and the first-order multiplicative model are shown in Fig. 4. While the stitch corrected with the zero-order model exhibits clearly visible intensity inhomogeneity resulting in poor segmentation performance, the results with the bias correction are notably better.

5 Discussion and Conclusions

In this work, we have presented a data-driven algorithm for performing different types of intensity correction for large EM panoramic images. The minimal assumptions our approach is based on allow its seamless extension to other modalities, including histopathology and magnetic resonance imaging.

Analysis of the intensity difference within the overlapping areas of the neighbouring frames confirms significantly improved results on the corrected data. Both models exhibit similar trend with respect to the order of the highest polynomial used for modelling the bias field, although this holds somewhat to a lesser extent for the multiplicative model. From the result presented in Fig. 2 we can conclude that, in this particular case, the bias field can be well modelled by a linear intensity gradient.

Training results exhibited a somewhat surprising trend, making it difficult to draw definite conclusions due to inconsistent performance of the three models on different validation data sets.

For solving the derived system of linear equations, it needs to be supported by a proper constraint(s). Although our current solution works well in practice, in the future research we will explore alternative, more natural, ways for conditioning the system.

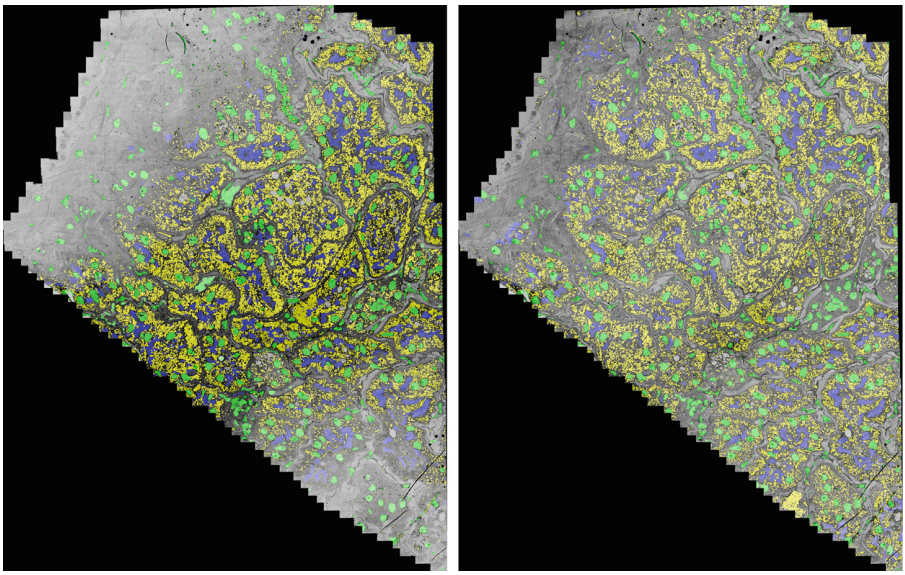

Fig. 4. Segmentation of the entire stitch for the data corrected by the zero-order (left) and the first-order multiplicative model (right); the segmentation masks are overlayed over the original images. Mitochondria, cell nuclei and ruffled border segmentation is shown in yellow, green and blue, respectively. (Color figure online)

Acknowledgment. We thank our colleagues Roman I. Koning, Aat A. Mulder, M. Christina Avramut and Frank G.A. Faas from the Department of Cell and Chemical Biology (LUMC) for their valuable contribution to this project. The tissue samples are courtesy of Ian Alwayn, Asel Arykbaeva and Dorottya de Vries from the Department of Surgery (LUMC).

Disclosure of Interests. This project was financed by the SAILS initiative of the Leiden University (Leiden, The Netherlands).

References

1. Bria, A., Iannello, G.: TeraStitcher – a tool for fast automatic 3D-stitching of teravoxel-sized microscopy images. BMC Bioinformatics **13**(1), 316 (2012)
2. Chalfoun, J., et al.: MIST: accurate and scalable microscopy image stitching tool with stage modeling and error minimization. Sci. Rep. **7**(1), 4988 (2017)
3. Coltuc, D., Bolon, P., Chassery, J.: Exact histogram specification. IEEE T. Image Process. **15**(5), 1143–1152 (2006)
4. Dzyubachyk, O., Koning, R.I., Mulder, A.A., Avramut, M.C., Faas, F.G.A., Koster, A.J.: Intensity correction and standardization for electron microscopy data. In: Heinrich, M.P., Dou, Q., de Bruijne, M., Lellmann, J., Schlaefer, A., Ernst, F. (eds.) Medical Imaging with Deep Learning, 7–9 July 2021, Lübeck, Germany. Proceedings of Machine Learning Research, vol. 143, pp. 148–157. PMLR (2021)

5. Faas, F.G., Avramut, M.C., van den Berg, B.M., Mommaas, A.M., Koster, A.J., Ravelli, R.B.: Virtual nanoscopy: generation of ultra-large high resolution electron microscopy maps. J. Cell Biol. **198**(3), 457–469 (2012)
6. Franco-Barranco, D., et al.: Current progress and challenges in large-scale 3D mitochondria instance segmentation. IEEE T. Med. Imaging **42**(12), 3956–3971 (2023)
7. Kaynig, V., Fischer, B., Müller, E., Buhmann, J.M.: Fully automatic stitching and distortion correction of transmission electron microscope images. J. Struct. Biol. **171**(2), 163–173 (2010)
8. Lahiani, A., Klaman, I., Navab, N., Albarqouni, S., Klaiman, E.: Seamless virtual whole slide image synthesis and validation using perceptual embedding consistency. IEEE J. Biomed. Health **25**, 403–411 (2021)
9. Li, C., Gore, J.C., Davatzikos, C.: Multiplicative intrinsic component optimization (MICO) for MRI bias field estimation and tissue segmentation. Magn. Reson. Med. **32**(7), 913–923 (2014)
10. Mahalingam, G., et al.: A scalable and modular automated pipeline for stitching of large electron microscopy datasets. eLife **11**, e76534 (2022)
11. Muhlich, J.L., Chen, Y.A., Yapp, C., Russell, D., Santagata, S., Sorger, P.K.: Stitching and registering highly multiplexed whole-slide images of tissues and tumors using ASHLAR. Bioinformatics **38**(19), 4613–4621 (2022)
12. Scheffer, L.K., Karsh, B., Vitaladevun, S.: Alignment of imperfect EM images for neural reconstruction. arXiv **1304.6034** (2013)
13. Xiao, C., et al.: Automatic mitochondria segmentation for EM data using a 3D supervised convolutional network. Front. Neuroanat. **12**, 92 (2018)
14. Zheng, Z., et al.: A complete electron microscopy volume of the brain of adult drosophila melanogaster. Cell **174**, 730-743.e22 (2018)